Article

Reconstruction of Bloch wavefunctions of holes in a semiconductor

https://doi.org/10.1038/s41586-021-03940-2

Received: 2 February 2021

Accepted: 20 August 2021

Published online: 3 November 2021

Check for updates

J. B. Costello[1,4], S. D. O'Hara[1,4], Q. Wu[1,4], D. C. Valovcin[2], L. N. Pfeiffer[3], K. W. West[3] & M. S. Sherwin[1]✉

A central goal of condensed-matter physics is to understand how the diverse electronic and optical properties of crystalline materials emerge from the wavelike motion of electrons through periodically arranged atoms. However, more than 90 years after Bloch derived the functional forms of electronic waves in crystals[1] (now known as Bloch wavefunctions), rapid scattering processes have so far prevented their direct experimental reconstruction. In high-order sideband generation[2–9], electrons and holes generated in semiconductors by a near-infrared laser are accelerated to a high kinetic energy by a strong terahertz field, and recollide to emit near-infrared sidebands before they are scattered. Here we reconstruct the Bloch wavefunctions of two types of hole in gallium arsenide at wavelengths much longer than the spacing between atoms by experimentally measuring sideband polarizations and introducing an elegant theory that ties those polarizations to quantum interference between different recollision pathways. These Bloch wavefunctions are compactly visualized on the surface of a sphere. High-order sideband generation can, in principle, be observed from any direct-gap semiconductor or insulator. We thus expect that the method introduced here can be used to reconstruct low-energy Bloch wavefunctions in many of these materials, enabling important insights into the origin and engineering of the electronic and optical properties of condensed matter.

Bloch's theorem tells us how to calculate both the Bloch wavefunctions and the spectrum of electronic energies (the 'band structure')[1]. A typical Bloch wave contains spatial oscillations with wavelengths ranging from atomic to macroscopic length scales. Of special interest is the low-energy, long-wavelength physics where the excited Bloch waves can be described by a finite-dimensional effective Hamiltonian (Methods). Knowledge about both the low-energy Bloch wavefunctions and band structure are essential to calculating the response of crystalline solids to most external stimuli. The band structure of many crystalline materials can be experimentally reconstructed from angle-resolved photoemission spectroscopy (ARPES) of electrons emitted from their surfaces[10,11]. ARPES enables determination of the energies of electronic waves as functions of their wavelengths and directions of propagation. However, there are no comparably direct methods to reconstruct Bloch wavefunctions. As a result, estimates of Bloch wavefunctions typically depend on parameters derived from the fits of complex models[12,13] to a few pieces of experimental data—such as the orbital frequency of an electron in a magnetic field (cyclotron resonance)[14]—that are sensitive only to averages over a range of electronic wave propagation directions and wavelengths. A key obstacle to directly probing Bloch wavefunctions in solids has been that, unlike molecules, where reconstructed electron wavefunctions have been reported[15–17], electronic waves in solids are typically distorted in a few picoseconds by scattering.

Recently, strong laser fields have been used to significantly accelerate electronic waves in solids before they are scattered. For example, high-harmonic generation has been demonstrated in solids[18–21] and led to an alternative method to probe band structures[22,23]. However, complicated interference between quantum pathways of electronic waves across multiple bands in high-harmonic-generation experiments[19] hinders the reconstruction of Bloch wavefunctions.

High-order sideband generation

Here we present a direct experimental reconstruction of Bloch wavefunctions of holes in bulk gallium arsenide (GaAs) using high-order sideband generation (HSG)[2–9]. In HSG, a relatively weak near-infrared (NIR) laser with frequency f_{NIR} and a strong laser with terahertz (THz) frequency f_{THz} simultaneously interact with a semiconductor, resulting in the emission of sideband photons with frequencies $f_{SB} = f_{NIR} + nf_{THz}$ where n is an integer. If the band structure is symmetric under inversion, as in the (001) plane of GaAs studied here, n must be even. HSG experiments have been conducted with both extremely narrow-band quasi-continuous-wave fields with $f_{THz} < 1$ THz, which have enabled the resolution of sidebands with $n > 60$ (ref. [7]), and broader-band pulsed fields with $f_{THz} > 10$ THz, which have enabled time resolution of the recollision process even in materials with dephasing times of less than 10 fs (ref. [5]). A quasi-continuous-wave HSG spectrum from bulk GaAs at 60 K is shown in Fig. 1a. In the experiment, a 100-mW NIR laser, and 2.01 ± 0.13 mJ, 40 ns, 0.447 ± 0.001 THz pulses generated by the University of California, Santa Barbara (UCSB) millimetre-wave free-electron

[1]Physics Department and Institute for Terahertz Science and Technology, University of California, Santa Barbara, Santa Barbara, CA, USA. [2]Mathworks, Natick, MA, USA. [3]Department of Electrical Engineering, Princeton University, Princeton, NJ, USA. [4]These authors contributed equally: J. B. Costello, S. D. O'Hara, Q. Wu. ✉e-mail: sherwin@ucsb.edu

laser[24] were linearly polarized and collinearly focused on a 500-nm GaAs epilayer (Fig. 1a, inset). The THz electric field strength in the epilayer was 70 ±2 kV cm^{-1} (Methods). In GaAs, HSG can be described by the following three-step process (Fig. 1b, Methods). First, electrons (E) and two species of hole—light holes (LH) and heavy holes (HH)—are created by the NIR laser. Second, the E–LH and E–HH pairs are driven apart and then back towards each other along the direction defined by the THz field (Fig. 1b). Crucially, during this acceleration phase, the Bloch waves associated with the E–LH and E–HH pairs interfere with each other. Third, they recollide with significant kinetic energy and emit sideband photons.

Information about the Bloch wavefunctions sampled by electrons and holes on their journeys through the Brillouin zone is imprinted on the polarization state of each sideband, which we measured by Stokes polarimetry (Methods). As light from a particular sideband can be associated with a quasi-momentum that is controlled by the THz field, its polarization will be different from the incoherent light emitted at the same energy in the absence of a strong THz field (photoluminescence), which is a superposition of emission from electron–hole pairs with all quasi-momenta satisfying energy conservation. The linear orientation angle, α, and the ellipticity angle, γ, for each sideband are shown in Fig. 1c for four different NIR polarizations. The polarizations of sidebands depend on the sideband index n and the NIR polarization in a manifestation of dynamical birefringence[6]. Although sideband intensities have a highly nonlinear dependence on THz power, they are proportional to the NIR power if it is sufficiently small[2]. All data reported here were taken in this regime of linear NIR response. In this linear regime, the sideband polarization can be mapped onto the polarization state of the NIR laser by a dynamical Jones matrix T (ref. [6]), defined in a basis of circularly polarized fields $\sigma^{\pm}$ (with helicity ±1) as

$$\begin{pmatrix} E_{+,n} \\ E_{-,n} \end{pmatrix} = \begin{pmatrix} T_{++,n} & T_{+-,n} \\ T_{-+,n} & T_{--,n} \end{pmatrix} \begin{pmatrix} E_{+,\mathrm{NIR}} \\ E_{-,\mathrm{NIR}} \end{pmatrix},$$

where $E_{\pm,n}$ and $E_{\pm,\mathrm{NIR}}$ denote the $\sigma^{\pm}$ components of the electric field associated with the nth sideband and NIR laser, respectively, and $T_{\pm\pm,n}$ denote the dynamical Jones matrix elements associated with the nth sideband. T-matrix elements were determined by measuring the sideband polarizations for four different linear NIR laser polarizations.

Dynamical Jones matrices

To understand the physics underlying each T-matrix element, it is necessary to consider the spins of electrons and holes. The four recollision pathways from the excitations generated by the $\sigma^{-}_{\mathrm{NIR}}$ component of the NIR laser are shown in Fig. 2. The electrons have spin 1/2, whereas the HHs and LHs have total spin 3/2. Driven by the THz field from time t' to t, an electron–hole pair acquires a dynamic phase

$$A_{\mathrm{HH(LH)}}(t', t) = -\int_{t'}^{t} \mathrm{d}t''(E_{\mathrm{c}}[\mathbf{k}(t'')] - E_{\mathrm{HH(LH)}}[\mathbf{k}(t'')])/\hbar,$$

where E_{c} and $E_{\mathrm{HH(LH)}}$ are the energies associated with the E and HH (LH) bands, respectively, shown schematically in Fig. 1b, $\mathbf{k}$ is the quasi-momentum and $\hbar$ is the reduced Planck's constant (Methods, Supplementary Discussion). The spin ±1/2 of the electron does not change during acceleration. As the Bloch wavefunctions in both the HH and the LH bands are superpositions of states with spin ±1/2 and spin ±3/2, the $\sigma^{-}_{\mathrm{NIR}}$ component can generate sidebands with either $\sigma^{-}_{\mathrm{HSG}}$ or $\sigma^{+}_{\mathrm{HSG}}$ while satisfying angular-momentum conservation, giving rise to dynamical Jones matrix elements $T_{--,n}$ and $T_{+-,n}$, respectively. Similar recollision pathways follow from the excitations generated by the $\sigma^{+}_{\mathrm{NIR}}$ component, giving rise to $T_{-+,n}$ and $T_{++,n}$ (Supplementary Discussion, Extended Data Fig. 4).

The properties of dynamical Jones matrices can be derived from the Luttinger Hamiltonian[25], which describes the physics of the HH and LH states at the relatively small energies and quasi-momenta probed in this experiment. We tune the NIR laser just below the bandgap and direct the THz field to propagate along the z axis to ensure the electrons and holes have no z component of quasi-momentum $\mathbf{k}$. In this case the Luttinger Hamiltonian takes a block diagonal form

$$\begin{aligned} H^{\pm}_{\mathrm{v}}(\mathbf{k}) &= -\frac{\hbar^2 k^2}{2m_0}\left[\gamma_1 \tau_0 - 2\gamma_2 \mathbf{n}_{\pm}\cdot\boldsymbol{\tau}\right] \\ &= -\frac{\hbar^2 k^2}{2m_0}\begin{pmatrix} \gamma_1+\gamma_2 & -\sqrt{3}(\gamma_2\sin(2\theta) \pm \mathrm{i}\gamma_3\cos(2\theta)) \\ -\sqrt{3}(\gamma_2\sin(2\theta) \mp \mathrm{i}\gamma_3\cos(2\theta)) & \gamma_1-\gamma_2 \end{pmatrix} \end{aligned} \quad (1)$$

where τ_0 is the identity matrix, $\boldsymbol{\tau}$ is the vector of Pauli matrices, θ is the angle between the THz field and the [110] crystal direction (Fig. 3d, inset), γ_1, γ_2 and γ_3 are the scalar Luttinger parameters, m_0 is the electron rest mass, and $\mathbf{n}_{\pm}$ is

$$\mathbf{n}_{\pm} = \left(\frac{\sqrt{3}}{2}\sin(2\theta), \mp\frac{\sqrt{3}\gamma_3}{2\gamma_2}\cos(2\theta), -\frac{1}{2}\right) \quad (2)$$

The Bloch wavefunctions are found by diagonalizing equation (1) and only depend on the $\mathbf{n}_{\pm}\cdot\boldsymbol{\tau}$ term because the first term is proportional to the identity. As $\mathbf{n}_{\pm}$ depends only on the crystal angle θ and γ_3/γ_2, an experimental measurement of γ_3/γ_2 allows the reconstruction of the Bloch wavefunctions. Even for $k_z \neq 0$, although the Luttinger Hamiltonian is not block diagonal, knowing γ_3/γ_2 is still sufficient to reconstruct the Bloch wavefunctions.

Reconstruction of Bloch wavefunctions

We use ratios of T-matrix elements to check the validity of the theory and measure γ_3/γ_2. As the diagonal elements of equation (1) are real, when sideband and NIR laser polarizations are the same, for each pathway producing a $\sigma^{+}_{\mathrm{HSG}}$ photon there is an equivalent pathway producing a $\sigma^{-}_{\mathrm{HSG}}$ photon (Fig. 2, Supplementary Discussion, Extended Data Fig. 4) through states related by time-reversal symmetry. Therefore, the ratio of diagonal dynamical Jones matrix elements for all sideband indices and crystal angles is

$$\frac{T_{++,n}(\theta)}{T_{--,n}(\theta)} \equiv \xi_n(\theta) = 1 \quad (3)$$

As the off-diagonal elements of equation (1) are complex, when sideband and NIR laser polarizations are different, for each pathway producing a $\sigma^{+}_{\mathrm{HSG}}$ photon there is an equivalent pathway producing a $\sigma^{-}_{\mathrm{HSG}}$ photon with a complex-conjugated phase factor (Supplementary Discussion). Therefore, the ratio of off-diagonal dynamical Jones matrix elements for all sideband indices is

$$\frac{T_{+-,n}(\theta)}{T_{-+,n}(\theta)} \equiv \chi_n(\theta) = \frac{\gamma_2\sin(2\theta) - \mathrm{i}\gamma_3\cos(2\theta)}{\gamma_2\sin(2\theta) + \mathrm{i}\gamma_3\cos(2\theta)} \quad (4)$$

The magnitude of $\chi_n(\theta)$ in equation (4) is 1 for all angles, but the argument depends on γ_3/γ_2 and θ.

The experimentally measured values $\chi_n(\theta)$ and $\xi_n(\theta)$ at various θ are compared with the predictions of equations (3) and (4) in Fig. 3 and Extended Data Fig. 5 using values for γ_3 and γ_2 recommended in ref. [13]. Within experimental error, $|\chi_n(\theta)|$ and $|\xi_n(\theta)|$ are 1, as predicted by equations (3) and (4) (Fig. 3a, Extended Data Fig. 5b, c). The arguments of $\chi_n(\theta)$ for eight different θ are independent of n (Fig. 3b), lying within 22° of the constant values predicted by equation 4 (dashed lines) for all θ except −45°. The values of $\chi(\theta) \equiv \langle\chi_n(\theta)\rangle$ and $\xi(\theta) \equiv \langle\xi_n(\theta)\rangle$, where averages are over n, are plotted at each θ in Fig. 3c, d. The magnitudes $|\chi(\theta)|$ and $|\xi(\theta)|$ are independent of θ, with a value of 1, as predicted by equations (3) and (4) (Fig. 3c). The argument of $\chi(\theta)$ is plotted with respect to θ in Fig. 3d, and is close to the prediction provided by

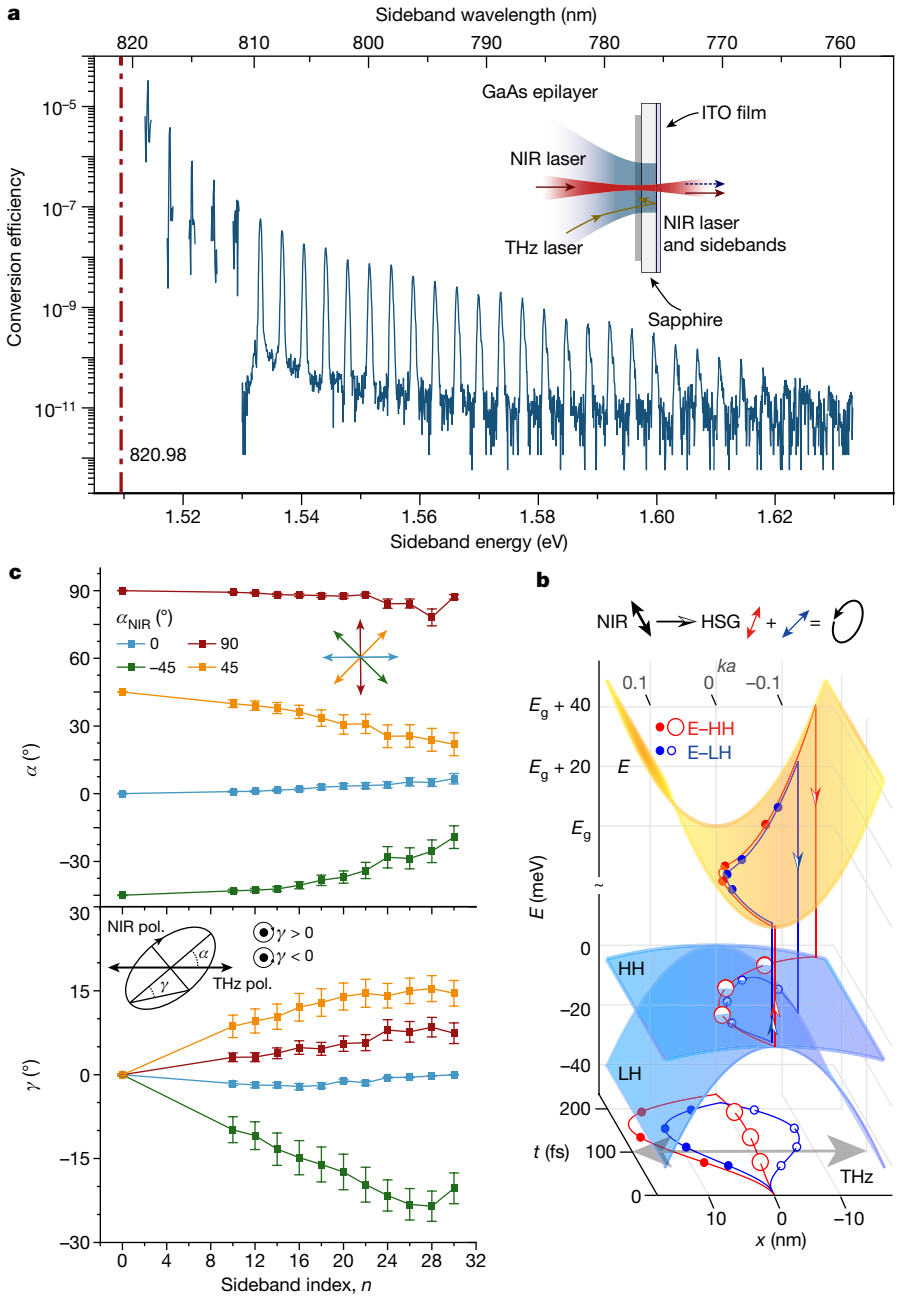

Fig. 1 | High-order sideband generation in bulk GaAs. a, An HSG spectrum (blue). The red dash-dot line indicates the NIR laser photon energy. Sidebands (peaks) are spaced by twice the THz frequency. Inset: experimental set-up schematic. **b**, Three-step model of HSG in GaAs. E–HH and E–LH recollision trajectories are denoted in red and blue, respectively, and are classical representations of interfering quantum pathways. The *y* axis (into page) corresponds to time. Bottom plane: real-space trajectories of E–HH and E–LH pairs. Three-dimensional mesh plot: *k*-space trajectories of the same pairs. The *z* axis corresponds to energy and the *x* axis corresponds to dimensionless quasi-momentum *ka*, where *a* is the lattice constant. Step 1: creation of E–HH and E–LH pairs by NIR laser (up arrows of equal length). Step 2: acceleration by the THz field. Electrons and holes begin at $k = 0$, and recollide with substantial kinetic energy at $|ka| > 0.1$. Step 3: recombination of E–HH and E–LH pairs and emission of sideband (down arrows of equal length). Top line: linearly polarized NIR laser photons (black double arrow) lead to emission of E–HH and E–LH sideband components (red and blue double arrows) with rotated linear polarizations and different phases, which combine to emit an elliptically polarized sideband. Classical calculations of trajectories (Methods) are for the 24th order sideband. **c**, Sideband linear orientation angle α and ellipticity angle γ as functions of sideband index for NIR laser linear orientation $\alpha_{NIR} = 0°$ (cyan), $\alpha_{NIR} = 90°$ (red), $\alpha_{NIR} = 45°$ (orange) and $\alpha_{NIR} = -45°$ (green) defined in upper inset. NIR laser polarization (pol.) angles are plotted as sidebands with $n = 0$. The lower inset defines α and γ with respect to the linearly polarized THz field. The measured polarization at each sideband index is displayed directly below the corresponding peak in the HSG spectrum in **a**. The error bars denote the standard deviation.

equation (4). Averaging the argument of $\chi(\theta)$ over experimentally sampled θ gives $\gamma_3/\gamma_2 = 1.47 \pm 0.48$, within experimental error of the value 1.42 recommended in ref. [13]. We attribute the deviations in measured $\chi_n(\theta)$ and $\xi_n(\theta)$ from theoretical predictions, as well as much of the experimental error in the determination of γ_3/γ_2, to small inhomogeneous strain in the GaAs membrane (Methods, Extended Data Fig. 2).

From γ_3/γ_2, we reconstruct the Bloch wavefunctions of the Luttinger Hamiltonian in GaAs. For two coupled bands, the Bloch wavefunctions can be represented as spinors on a Bloch sphere[26]. In the $k_z = 0$ plane,

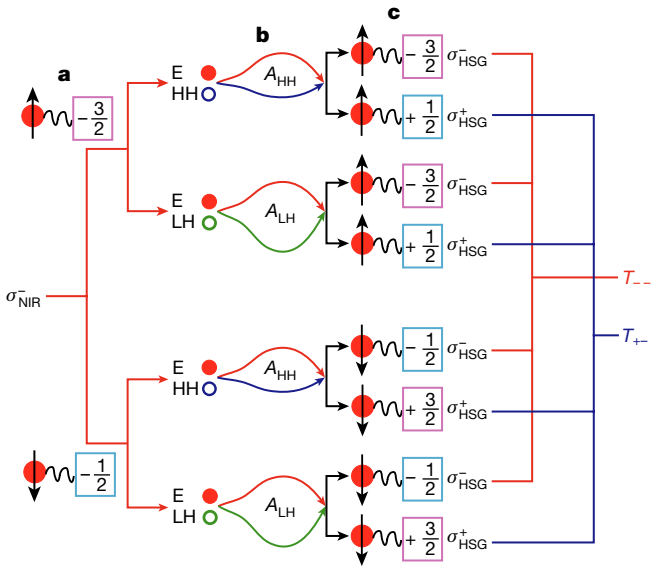

Fig. 2 | Quantum interference leading to sideband polarization. A photon from the NIR laser is decomposed into components $\sigma^{\pm}_{NIR}$, with helicity ±1. **a**, A σ^-_{NIR} photon excites either a spin-up electron and hole of spin −3/2 or a spin-down electron and hole of spin −1/2. **b**, Driven by the THz field, an electron–hole pair accumulates dynamic phase A_{HH} or A_{LH}, depending on the band of the hole state (HH or LH). The electron spin is unchanged, whereas the hole states originating from the spin −3/2 state are superpositions of spin −3/2 and +1/2 states and the states originating from the spin −1/2 state are superpositions of spin −1/2 and +3/2 states. **c**, Upon recollision, either σ^+_{HSG} or σ^-_{HSG} photons are produced following angular momentum conservation—for example, a spin +3/2 hole recombining with a spin-down (−1/2) electron produces a σ^+_{HSG} photon with helicity +3/2 −1/2 = +1. The interference of the evolution pathways from σ^-_{NIR} to σ^+_{HSG} (σ^-_{HSG}) produces the dynamical Jones matrix element T_{+-} (T_{--}). Photons with σ^+_{NIR} result in similar pathways to produce to T_{-+} and T_{++} (Supplementary Discussion, Extended Data Fig. 4).

each block of the Luttinger Hamiltonian is a two-by-two matrix, whose eigenfunctions—the Bloch wavefunctions—depend on θ but not on $|\mathbf{k}| = k$. Thus, in the $k_z = 0$ plane, for any θ, a single point on the Bloch sphere represents the Bloch wavefunctions for arbitrary k. The closed black curves in the northern and southern hemispheres of the Bloch sphere in Fig. 4 represent the most likely Bloch wavefunctions consistent with our measured γ_3/γ_2 for the LH and HH, respectively. The north and south poles represent the states with spin −3/2 and +1/2, respectively. The Bloch wavefunctions for the degenerate partners of those represented in Fig. 4 are related by time-reversal symmetry.

Discussion

The complete electronic structure of a crystalline solid should include both its band structure and Bloch wavefunctions. We have reconstructed low-energy Bloch wavefunctions of holes in GaAs from polarimetry of high-order sideband spectra. GaAs is one of the most widely studied semiconductors, and the consistency of our results with the vast body of complementary previous work validates the novel method presented here. HSG can, in principle, be observed from any direct-gap semiconductor or insulator, and has been observed in semiconductor quantum wells[2,3,6,7] and both monolayer and bulk semiconducting transition metal dichalchogenides[5,8,9]. Thus, we expect polarimetry of high-order sidebands can be measured from a large class of bulk and nanostructured materials. As a probe of electronic structure, the sensitivity of HSG to the bulk of electrically insulating materials has the potential to complement ARPES, which works best on surfaces.

Holes in GaAs are an interesting special case because the Luttinger Hamiltonian is one of the simplest non-trivial, low-energy effective Hamiltonians in solids. However, HSG spectra contain a wealth of information about the portions of the Brillouin zone explored during the acceleration phase, and straightforward extensions of the work presented here will enable reconstruction of Bloch wavefunctions from a wide range of low-energy Hamiltonians. Each peak in a HSG spectrum can be thought of as the output of an interferometer for Bloch waves. During acceleration by the THz field, Bloch wavepackets generally accumulate two types of phase: dynamic phases $A_{HH(LH)}$, which have been extensively discussed here, and geometric phases (also called Berry phases)[6]. Dynamic phases depend on only the time-dependent energy eigenvalues of electrons and holes during acceleration. Geometric phases accumulate if the Bloch wavefunctions of electrons or holes change along their trajectories. The Luttinger model predicts

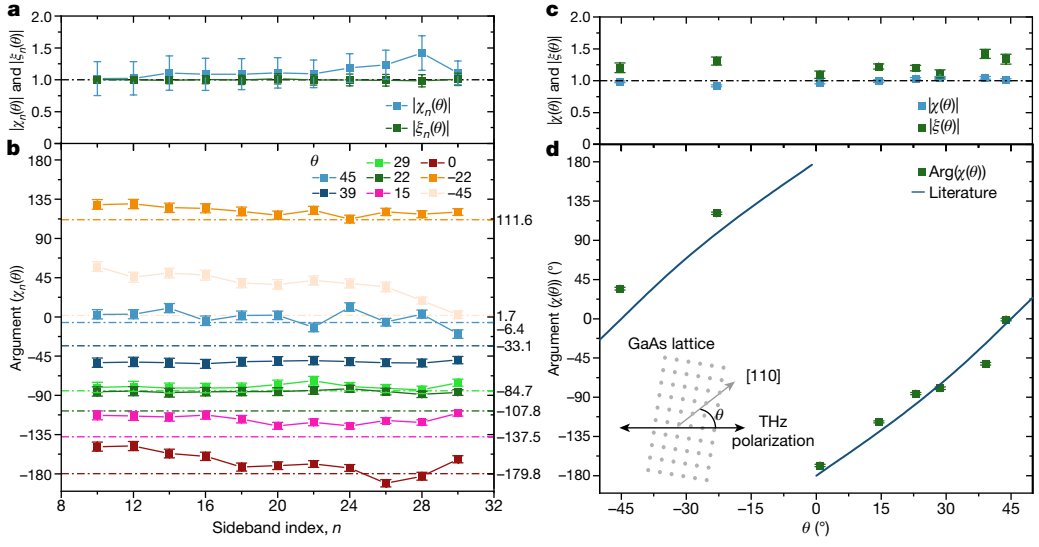

Fig. 3 | Ratios of Jones matrix elements, $\xi_n(\theta) \equiv T_{++,n}(\theta)/T_{--,n}(\theta)$ and $\chi_n(\theta) \equiv T_{+-,n}(\theta)/T_{-+,n}(\theta)$, measured by Stokes polarimetry. a, The magnitude of $\chi_n(\theta)$ and $\xi_n(\theta)$ at $\theta = 39°$. The dash-dot line marks the magnitude of 1 predicted by equation (3). For other θ, see Extended Data Fig. 5. **b**, The argument of $\chi_n(\theta)$ as a function of sideband index n, at various θ. The dash-dot lines mark the expected values (noted on the right) from equation (4), using values of γ_2 and γ_3 recommended in ref. [13]. **c**, The magnitudes of $\chi(\theta) \equiv \langle\chi_n(\theta)\rangle$ and $\xi(\theta) \equiv \langle\xi_n(\theta)\rangle$ averaged over sideband index n. The dash-dot line indicates the magnitude of 1 predicted by equations (3) and (4). **d**, The argument of $\chi(\theta)$ at each experimentally probed θ. The solid blue line is the expected argument from equation (4) using the values of γ_2 and γ_3 recommended in ref. [13]. Inset: the definition of θ, using the GaAs crystal lattice and the THz electric field. Error bars denote one standard deviation.

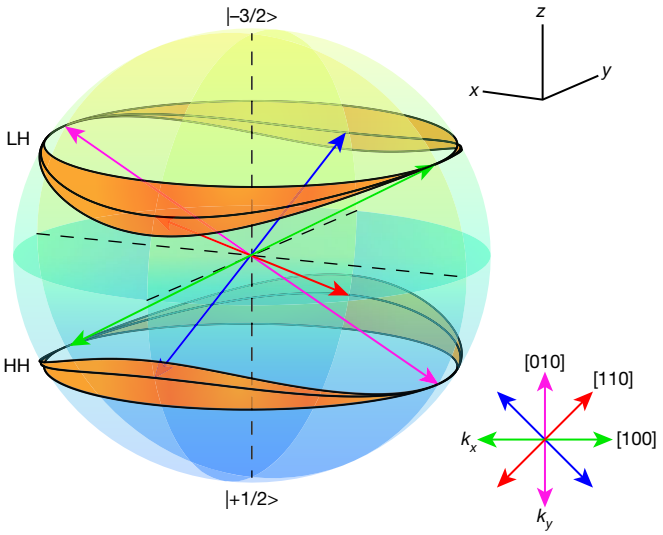

Fig. 4 | Reconstruction of the Bloch wavefunctions for $k_z = 0$. The Bloch wavefunctions of HH and LH bands associated with H_+ in equation (1) are plotted as black lines. The orange shaded area corresponds to the uncertainty in the wavefunction associated with one standard deviation in the measurement of γ_2/γ_3. For a given θ, each wavefunction is represented by a point on the Bloch sphere. The arrows within the Bloch sphere point from the origin to the LH and HH Bloch wavefunctions for the values of θ defined by their Miller indices in the inset below. The poles correspond to the spin −3/2 and spin +1/2 states. The wavefunctions for H_- are paths reflected across the x–z plane on a Bloch sphere with poles representing the spin +3/2 and spin −1/2 states.

that, along special trajectories that are straight lines through the Γ point oriented along the constant angle θ defined by the linearly polarized THz electric field, electron–hole pairs acquire dynamic phases $A_{HH(LH)}$, but no Berry phases (Supplementary Discussion, Extended Data Fig. 7). Experimental conditions (linearly polarized THz electric field and NIR excitation with $\mathbf{k} = 0$) were chosen to excite only such trajectories to simplify analysis. However, in Hamiltonians with lower symmetry, even for these simple experimental conditions, Berry phases will, in general, accumulate during acceleration. For example, the addition of a small biaxial strain to GaAs lowers the symmetry, splits degeneracy between HH and LH bands at the Γ point, and makes it inevitable that both dynamic and non-Abelian Berry phases contribute to the intensity and polarization of sidebands (Supplementary Discussion, Extended Data Fig. 8). We are currently investigating the hypothesis that the imperfect agreement between experiment and theory in Fig. 3 is due to small strains in this sample.

We expect Bloch wavefunctions of nearly degenerate bands can be reconstructed for a wide range of semiconducting and insulating materials by minimizing the difference between measured Jones matrix elements and those predicted by the appropriate effective Hamiltonian. We anticipate the following requirements on materials and light sources to enable Bloch wavefunction reconstruction. The carrier density should be sufficiently low that it does not interfere with the recollision process. One must know the space group of the material and the spin and orbital angular momenta associated with each of the optically excited bands at the band edge to construct a low-energy effective Hamiltonian with the correct symmetry and set of parameters using $\mathbf{k} \cdot \mathbf{p}$ theory. The laser tuned to the bandgap of the material should be sufficiently weak that sideband intensities are in the linear regime. The strong THz laser should have sufficiently narrow bandwidth and low-enough frequency to resolve multiple sidebands in the portion of the Brillouin zone of interest. The THz electric field should be strong enough to ionize electron–hole pairs in a fraction of a cycle, and for acceleration and recollision to occur for a detectable fraction of photo-excited quasiparticles before scattering disrupts the process, but not so strong that it creates electron–hole pairs spontaneously. By leveraging a variety of state-of-the-art narrow-band THz sources[27], we believe that Bloch wavefunction reconstruction from polarimetry of high-order sidebands can become an important technique for determining the complete low-energy electronic structure of charged quasiparticles in both weakly and strongly correlated materials.

Online content

Any methods, additional references, Nature Research reporting summaries, source data, extended data, supplementary information, acknowledgements, peer review information; details of author contributions and competing interests; and statements of data and code availability are available at https://doi.org/10.1038/s41586-021-03940-2.

1. Bloch, F. *Über die quantenmechanik der elektronen in kristallgittern*. *Z. Phys.* **52**, 555–600 (1929).
2. Zaks, B., Liu, R. B. & Sherwin, M. S. Experimental observation of electron–hole recollisions. *Nature* **483**, 580–583 (2012).
3. Banks, H. et al. Terahertz electron–hole recollisions in GaAs/AlGaAs quantum wells: robustness to scattering by optical phonons and thermal fluctuations. *Phys. Rev. Lett.* **111**, 267402 (2013).
4. Zaks, B., Banks, H. & Sherwin, M. S. High-order sideband generation in bulk GaAs. *Appl. Phys. Lett.* **102**, 012104 (2013).
5. Langer, F. et al. Lightwave-driven quasiparticle collisions on a subcycle timescale. *Nature* **533**, 225–229 (2016).
6. Banks, H. B. et al. Dynamical birefringence: electron–hole recollisions as probes of Berry curvature. *Phys. Rev. X* **7**, 041042 (2017).
7. Valovcin, D. C. et al. Optical frequency combs from high-order sideband generation. *Opt. Express* **26**, 29807–29816 (2018).
8. Langer, F. et al. Lightwave valleytronics in a monolayer of tungsten diselenide. *Nature* **557**, 76–80 (2018).
9. Borsch, M. et al. Super-resolution lightwave tomography of electronic bands in quantum materials. *Science* **370**, 1204–1207 (2020).
10. Yang, H. F. et al. Visualizing electronic structures of quantum materials by angle-resolved photoemission spectroscopy. *Nat. Rev. Mater.* **3**, 341–353 (2018).
11. Damascelli, A., Hussain, Z. & Shen, Z. X. Angle-resolved photoemission studies of the cuprate superconductors. *Rev. Mod. Phys.* **75**, 473–541 (2003).
12. Lawaetz, P. Valence-band parameters in cubic semiconductors. *Phys. Rev. B* **4**, 3460–3467 (1971).
13. Vurgaftman, I., Meyer, J. R. & Ram-Mohan, L. R. Band parameters for III–V compound semiconductors and their alloys. *J. Appl. Phys.* **89**, 5815–5875 (2001).
14. Skolnick, M. S. et al. An investigation of anisotropy of valence band of GaAs by cyclotron-resonance. *J. Phys. C* **9**, 2809–2821 (1976).
15. Itatani, J. et al. Tomographic imaging of molecular orbitals. *Nature* **432**, 867–871 (2004).
16. Luftner, D. et al. Imaging the wave functions of adsorbed molecules. *Proc. Natl Acad. Sci. USA* **111**, 605–610 (2014).
17. Shafir, D., Mairesse, Y., Villeneuve, D. M., Corkum, P. B. & Dudovich, N. Atomic wavefunctions probed through strong-field light-matter interaction. *Nat. Phys.* **5**, 412–416 (2009).
18. Ghimire, S. & Reis, D. A. High-harmonic generation from solids. *Nat. Phys.* **15**, 10–16 (2019).
19. Hohenleutner, M. et al. Real-time observation of interfering crystal electrons in high-harmonic generation. *Nature* **523**, 572–575 (2015).
20. Ghimire, S. & Reis, D. A. High-harmonic generation from solids. *Nat. Phys.* **15**, 10–16 (2019).
21. Liu, H. Z. et al. High-harmonic generation from an atomically thin semiconductor. *Nat. Phys.* **13**, 262–265 (2017).
22. Vampa, G. et al. All-optical reconstruction of crystal band structure. *Phys. Rev. Lett.* **115**, 193603 (2015).
23. Luu, T. T. et al. Extreme ultraviolet high-harmonic spectroscopy of solids. *Nature* **521**, 498–502 (2015).
24. Ramian, G. The new UCSB free-electron lasers. *Nucl. Instrum. Methods Phys. A* **318**, 225–229 (1992).
25. Luttinger, J. M. & Kohn, W. Motion of electrons and holes in perturbed periodic fields. *Phys. Rev.* **97**, 869–883 (1955).
26. Bernevig, B. A., Hughes, T. L. & Zhang, S. C. Quantum spin Hall effect and topological phase transition in HgTe quantum wells. *Science* **314**, 1757–1761 (2006).
27. Fulop, J. A., Tzortzakis, S. & Kampfrath, T. Laser-driven strong-field terahertz sources. *Adv. Opt. Mater.* **8**, 1900681 (2020).

Methods

Fabrication of GaAs sample

A 500-nm-thick GaAs epilayer was grown via molecular beam epitaxy and then transferred onto a sapphire substrate through van der Waals bonding[28–31]. The sapphire was transparent to both NIR and THz radiation. The fact that the thermal expansion coefficients of sapphire and GaAs are closely matched ensures relatively small strains in the GaAs epilayer upon thermal cycling. To make the strain as small and homogeneous as possible, the GaAs epilayer was etched to be circular. A layer of indium tin oxide (ITO)—which reflects THz radiation while transmitting NIR radiation—was grown on the sapphire surface that was opposite to the GaAs epilayer to create a low-quality-factor cavity that enhanced the THz field in GaAs at selected THz frequencies. At the 447 GHz frequency used in this study, the THz field is enhanced by a factor of 1.5 from the ITO layer (Extended Data Fig. 1). A silicon dioxide (SiO_2) anti-reflection coating was grown on top of the ITO to minimize its NIR reflection and avoid NIR Fabry–Perot oscillations in the sideband spectra. See Supplementary Methods for a step-by-step fabrication procedure.

The absorbance spectra of the GaAs epilayer were measured in a cryogenic chamber as a preliminary characterization on strains, as well as the excitation gap, which motivated our choice of NIR laser wavelengths for HSG experiments. Extended Data Fig. 2 shows an absorbance spectrum measured at a sample temperature of 60 K using a white light source, and calculated as $A = -10$ log(Transmitted power with sample in cryostat/Transmitted power with cryostat (and sample) removed). The sharp peaks are assigned to exciton resonances associated with band-edge states with different angular momenta. These peaks are separated by 2.6 meV. A recent study has associated a similar splitting with a strain of order 0.1% (ref. [32]). The absorbance spectra in the immediate neighbourhood of the illuminated spot chosen for the HSG experiments in this study showed little variation.

Optical methods

The NIR laser was generated from an M Squared SolTiS titanium:sapphire laser, with a 7-W, 532-nm Sprout laser as the pump. The M Squared cavity is tunable via piezoelectric response, with a precision of 0.01-Å output NIR wavelength, measured in real time by a WS6-600 wavemeter. The linewidth of the SolTiS is less than 5 MHz, enabling excitation of electron–hole pairs with very well defined energy and contributing negligibly to sideband linewidth, which is determined primarily by pulse-to-pulse fluctuations in the free-electron-laser (FEL) frequency[7]. An acousto-optic modulator was used to direct the NIR laser onto the sample for 1 μs at a 0.0001% duty cycle, synchronized with the THz output pulse from the FEL. After the modulation, only the first-order beam propagated through the rest of the optical elements. The polarization of the NIR laser beam incident onto the GaAs epilayer was set with a quarter-wave plate and a half-wave plate, and measured by a Thorlabs PAX polarimeter. The NIR beam was focused down to about 500 μm at the GaAs epilayer using a 500-mm lens.

The THz radiation was generated from the cavity-dumped UCSB millimetre-wave free-electron laser[24,33,34]. Most of the variance in the output frequency was due to variance in the terminal voltage of the electrostatic accelerator that drives the FEL[7]. The THz beam output from an optical transport system was split into two beam paths. Ten per cent of the THz output power was directed into a fast-response pyroelectric reference detector, which measured the output power of each FEL pulse. The other 90% of the THz output power was directed onto the cryostat containing the GaAs epilayer. A 12.5-cm, gold-coated off-axis parabolic mirror was used to focus the THz beam into a 1.2-mm-diameter spot. An ITO slide, which was transmissive in the NIR but reflective in the THz range, was used to adjust the THz beam spot on the GaAs epilayer and make sure that the NIR and THz fields were collinear. The pulse energy was measured on each day before the HSG experiments using a Thomas Keating absolute power/energy meter placed after the beam splitter but before the parabolic mirror. The pulse energy measured by the Thomas Keating power meter was used to calibrate the fast pyroelectric reference detector.

The THz field strength in the GaAs epilayer is estimated to be 70 ± 2 kV cm^{-1}. This high THz field strength resulted in the large number of sidebands reported here. However, the dependence of sideband polarization angles on NIR laser polarization angles measured at fields as low as 35 kV cm^{-1} was similar to the dependence reported in Fig. 1c. In the calculation of THz field strength, we assume that the gold-coated off-axis parabolic mirror is 100% reflective, the ITO slide is 70% reflective, the cryostat window is 95% transmissive and the ITO coating on the sapphire provides a 150% field enhancement on the sample.

The sidebands generated from the GaAs sample were first transmitted through a Stokes polarimeter, which includes a rotating quarter-wave plate (RQWP) and a horizontal linear polarizer. The Stokes polarimeter was calibrated by measuring the NIR laser polarizations with the Thorlabs PAX polarimeter, which was impractical for Stokes polarimetry of the sidebands because it is optimized for use with a continuous-wave laser beam at a single frequency. The intensity of each sideband was measured either by a photomultiplier tube or a charge-coupled device (CCD), each coupled to a dedicated monochromator[6]. The photomultiplier tube measured the lowest-order sidebands, while the CCD imaged many higher-order sidebands simultaneously. To optimize the efficiencies of the diffraction gratings, a half-wave plate was placed after the Stokes polarimeter to rotate the sideband polarizations.

All measurements were performed at 60 K, which was the base temperature of the cryostat during this experimental campaign. HSG polarimetry spectra recorded at lower temperatures were similar to those reported here.

Extraction of γ_3/γ_2 from Stokes polarimetry

We characterize the polarization of each sideband using the four Stokes parameters defined as $S_0 = I$, $S_1 = Ip\cos 2\alpha\cos 2\gamma$, $S_2 = Ip\sin 2\alpha\cos 2\gamma$ and $S_3 = Ip\sin 2\gamma$, where I is the total intensity, p is the degree of polarization, and the orientation angle α and ellipticity angle γ are defined in the inset of Extended Data Fig. 3b. After a sideband passes through the RQWP and horizontal linear polarizer, the intensity of the outgoing light, $S_{\mathrm{out}}(\phi)$, can be expressed as

$$S_{\mathrm{out}}(\phi) = \frac{S_0}{2} + \frac{S_1}{4} - \frac{S_3}{2}\sin(2\phi) + \frac{S_1}{4}\cos(4\phi) + \frac{S_2}{4}\sin(4\phi)$$

where ϕ is the angle between the fast-axis of the RQWP and the horizontal. By measuring S_{out} as a function of ϕ, the four Stokes parameters can be extracted from the Fourier transform $\mathcal{F}_m = \int_0^{2\pi} S_{\mathrm{out}}(\phi)e^{-im\phi}d\phi/2\pi$: $S_0 = 2\mathcal{F}_0 - 4\mathrm{Re}(\mathcal{F}_4)$, $S_1 = 8\mathrm{Re}(\mathcal{F}_4)$, $S_2 = -8\mathrm{Im}(\mathcal{F}_4)$ and $S_3 = 4\mathrm{Im}(\mathcal{F}_2)$. We sampled the intensities of each sideband at 16 different angles ϕ. We define plots of S_{out} as functions of the angle ϕ as 'polaragrams' (see Extended Data Fig. 3a, c for examples). For each angle ϕ, four CCD scans were taken to establish the variance of the intensity S_{out}. From the Stokes parameters of the nth-order sideband, $S_{i,n}$, the polarization state of the sideband can be extracted by calculating the angles α_n and γ_n from relations

$$\tan(2\alpha_n) = \frac{S_{2,n}}{S_{1,n}}$$

$$\tan(2\gamma_n) = \frac{S_{3,n}}{\sqrt{S_{1,n}^2 + S_{2,n}^2}}$$

Examples of extracted polarization states of sidebands are shown in Extended Data Fig. 3b, d.

To reconstruct the dynamical Jones matrices, the polarization states of the sidebands were measured for four different polarization states

of the NIR laser. All polarizations of the NIR laser were linear ($\gamma_{NIR} = 0°$) with orientation angles $\alpha_{NIR} = 0°$, $\alpha_{NIR} = 45°$, $\alpha_{NIR} = 90°$ and $\alpha_{NIR} = -45°$, respectively. Each dynamical Jones matrix $\mathcal{J}$ connects the electric fields of the NIR laser and a sideband through

$$\begin{pmatrix} E_{x,n} \\ E_{y,n} \end{pmatrix} = \begin{pmatrix} \mathcal{J}_{xx,n} & \mathcal{J}_{xy,n} \\ \mathcal{J}_{yx,n} & \mathcal{J}_{yy,n} \end{pmatrix} \begin{pmatrix} E_{x,\mathrm{NIR}} \\ E_{y,\mathrm{NIR}} \end{pmatrix}$$

where

$$\begin{pmatrix} E_{x,n} \\ E_{y,n} \end{pmatrix} = \begin{pmatrix} \cos\alpha_n & -\sin\alpha_n \\ \sin\alpha_n & \cos\alpha_n \end{pmatrix} \begin{pmatrix} \cos\gamma_n \\ i\sin\gamma_n \end{pmatrix} \equiv \begin{pmatrix} \cos\beta_n \\ e^{i\delta_n}\sin\beta_n \end{pmatrix} e^{i\zeta_n}$$

$$\begin{pmatrix} E_{x,\mathrm{NIR}} \\ E_{y,\mathrm{NIR}} \end{pmatrix} = \begin{pmatrix} \cos\alpha_{\mathrm{NIR}} & -\sin\alpha_{\mathrm{NIR}} \\ \sin\alpha_{\mathrm{NIR}} & \cos\alpha_{\mathrm{NIR}} \end{pmatrix} \begin{pmatrix} \cos\gamma_{\mathrm{NIR}} \\ i\sin\gamma_{\mathrm{NIR}} \end{pmatrix} \equiv \begin{pmatrix} \cos\beta_{\mathrm{NIR}} \\ e^{i\delta_{\mathrm{NIR}}}\sin\beta_{\mathrm{NIR}} \end{pmatrix} e^{i\zeta_{\mathrm{NIR}}}$$

The ratio $E_{y,n}/E_{x,n}$ yields the equation

$$\cos\beta_n \left(\frac{\mathcal{J}_{yx,n}}{\mathcal{J}_{xx,n}} \cos\beta_{\mathrm{NIR}} + \frac{\mathcal{J}_{yy,n}}{\mathcal{J}_{xx,n}} e^{i\delta_{\mathrm{NIR}}} \sin\beta_{\mathrm{NIR}} \right) - e^{i\delta_n} \sin\beta_n \left(\cos\beta_{\mathrm{NIR}} + \frac{\mathcal{J}_{xy,n}}{\mathcal{J}_{xx,n}} e^{i\delta_{\mathrm{NIR}}} \sin\beta_{\mathrm{NIR}} \right) = 0$$

which is linear with respect to the ratios $\mathcal{J}_{yx,n}/\mathcal{J}_{xx,n}$, $\mathcal{J}_{yy,n}/\mathcal{J}_{xx,n}$ and $\mathcal{J}_{xy,n}/\mathcal{J}_{xx,n}$. Measurements for three polarization states of the NIR laser give three such linear equations, which uniquely determine the ratios between the dynamical Jones matrix elements. From the measurements for the four NIR polarizations, we obtained four linear equations, which were solved by the method of least squares. The absolute values of the dynamical Jones matrix elements, which are not concerns of this study, can be determined through the absolute values of the Stokes parameters.

Each dynamical Jones matrix $\mathcal{J}$ was converted to the T-matrix in a basis of circular polarizations through unitary transformation $T = U^{\dagger}\mathcal{J}U$, where

$$U = \frac{1}{\sqrt{2}} \begin{pmatrix} e^{-i\varphi} & -e^{i\varphi} \\ ie^{-i\varphi} & ie^{i\varphi} \end{pmatrix}$$

Here, φ is the angle between the THz polarization and the [100] crystal direction.

From equation (4), with the measured T-matrix, the ratio γ_3/γ_2 can be calculated as

$$\frac{\gamma_3}{\gamma_2} = |\tan 2\theta| \sqrt{\frac{1 - \cos\mathrm{Arg}(T_{+-,n}/T_{-+,n})}{1 + \cos\mathrm{Arg}(T_{+-,n}/T_{-+,n})}}$$

where $\mathrm{Arg}(T_{+-,n}/T_{-+,n})$ is the argument of $T_{+-,n}/T_{-+,n}$, and θ is the angle between the THz polarization and the [110] crystal direction. From each angle θ ($\sin 2\theta, \cos 2\theta \neq 0$) and the ratio $T_{+-,n}/T_{-+,n}$ for each sideband, one value of γ_3/γ_2 was obtained. An average over sideband index n and angle θ yields $\gamma_3/\gamma_2 = 1.47 \pm 0.48$, where the quoted error is the standard deviation of γ_3/γ_2.

A Monte Carlo simulation was performed to estimate the errors in the dynamical Jones matrix elements from two sources, which were added in quadrature: (1) the variance in the sideband intensity measurements and (2) the deviation $\delta\eta$ of RQWP retardance η from its ideal value $\pi/2$. A small deviation $\delta\eta$ in the RQWP retardance modifies the relations between the Fourier transforms $\mathcal{F}_m$ and Stokes parameters as: $S_0 = 2\mathcal{F}_0 - 4\mathrm{Re}(\mathcal{F}_4)(1 - \delta\eta)/(1 + \delta\eta)$, $S_1 = 8\mathrm{Re}(\mathcal{F}_4)/(1 + \delta\eta)$, $S_2 = -8\mathrm{Im}(\mathcal{F}_4)/(1 + \delta\eta)$ and $S_3 = 4\mathrm{Im}(\mathcal{F}_2)/(1 - \delta\eta^2/2)$. The deviation $\delta\eta$ was calibrated to be in the range $[-\pi/36, \pi/36]$. The angles α_n and γ_n of the nth-order sideband were randomly sampled from normal distributions, with the mean and standard deviation set as the measured mean values and errors as shown in Extended Data Fig. 6a. Each set of α_n and γ_n were sampled 10,000 times, generating 10,000 values for each of the dynamical Jones matrix elements. As an example, Extended Data Fig. 6b shows the distribution of 1,000 sets of α_{12} and γ_{12} for four polarization states of the NIR laser. The value and error of each dynamical Jones matrix element was calculated as the mean and the standard deviation of the generated distribution, respectively. Note that the dynamical Jones matrix elements are complex valued, and we set $\mathcal{J}_{xx,n} = 1$ in this study. Extended Data Fig. 6c shows the distributions of the dynamical Jones matrix elements produced from the distributions of α_{12} and γ_{12} in Extended Data Fig. 6b.

Effective Hamiltonian and low-energy Bloch wavefunctions

In the basis consisting the eigenvectors of the position operator $\hat{\mathbf{r}}$, a Bloch wavefunction with band index N and quasi-momentum $\mathbf{k}$ has the form $\langle \mathbf{r}|\psi_{N,\mathbf{k}}\rangle = e^{i\mathbf{k}\rangle\mathbf{r}} u_{N,\mathbf{k}}(\mathbf{r})$, where $u_{N,\mathbf{k}}(\mathbf{r}) = \langle \mathbf{r}|u_{N,\mathbf{k}}\rangle$ is a periodic function with the periodicity of the crystal. The eigenvalue problem of the Bloch wave functions, $H|\psi_{N,\mathbf{k}}\rangle = E_{N,\mathbf{k}}|\psi_{N,\mathbf{k}}\rangle$, can be equivalently stated as an eigenvalue problem of the state $|u_{N,\mathbf{k}}\rangle$ in the form $H(\mathbf{k})|u_{N,\mathbf{k}}\rangle = E_{N,\mathbf{k}}|u_{N,\mathbf{k}}\rangle$, where $H(\mathbf{k}) \equiv e^{-i\mathbf{k}\cdot\hat{\mathbf{r}}} H e^{i\mathbf{k}\cdot\hat{\mathbf{r}}}$. According to the $\mathbf{k}\cdot\mathbf{p}$ method[35], in cases where the excited Bloch waves are located in energy bands that are relatively isolated and their quasi-momenta are restricted in a small portion of the Brillouin zone, a finite number of states $|u_{N,\mathbf{k}_0}\rangle$ at quasi-momentum $\mathbf{k}_0$ can be approximately taken as a complete basis. On this finite basis, the Hamiltonian $H(\mathbf{k})$ can be represented as a finite-dimensional matrix—the effective Hamiltonian, whose eigenfunctions, the low-energy Bloch wavefunctions, are linear combinations of the states $\{|u_{N,\mathbf{k}_0}\rangle\}$. Determination of the effective Hamiltonian does not rely on the exact representations of the states $\{|u_{N,\mathbf{k}_0}\rangle\}$ in real-space coordinates but their symmetry properties. The Luttinger Hamiltonian is an effective Hamiltonian with the basis chosen as four valence-band-edge states (Supplementary Discussion).

Interference of Bloch waves

We consider the case where the photon energy of the NIR laser lies just below the bandgap and assume that the sideband amplitudes are dominantly determined by electron–hole pairs created at $\mathbf{k} = \mathbf{0}$. Under an approximation of free electrons and holes, the amplitude of the nth sideband can be written as (Supplementary Discussion)

$$\mathbb{P}_n = \sum_{s=\pm} \frac{i\omega}{2\pi V\hbar} \int_0^{2\pi/\omega} dt e^{i(\Omega+n\omega)t} \int_{-\infty}^{t} dt' \mathbb{D}_s^{\dagger} R_s \begin{pmatrix} e^{iA_{\mathrm{HH}}(t',t)} & 0 \\ 0 & e^{iA_{\mathrm{LH}}(t',t)} \end{pmatrix} R_s^{\dagger} \mathbb{D}_s \cdot \mathbf{E}_{\mathrm{NIR}}(t')$$

where ω and Ω are the angular frequencies of the THz field and the NIR laser, respectively, V is the volume of the material, $\mathbf{E}_{\mathrm{NIR}}(t) = \mathbf{F}_{\mathrm{NIR}} e^{-i\Omega t}$ is the electric field of the NIR laser under the rotating wave approximation, the two components of $\mathbb{D}_+ = -d(\boldsymbol{\sigma}_-, \boldsymbol{\sigma}_+/\sqrt{3})^T$ ($\mathbb{D}_- = -d(\boldsymbol{\sigma}_+, \boldsymbol{\sigma}_-/\sqrt{3})^T$) are dipole matrix elements between spin-down (spin-up) electron and hole states with spin +3/2 (−3/2) and spin −1/2 (+1/2), respectively (d is a constant dipole matrix element), and $R_\pm$ is a two-by-two unitary matrix that diagonalizes the hole Hamiltonian $[H_v^{\pm}(\mathbf{k})]^*$ through $R_\pm^{\dagger}(\hat{\mathbf{n}}_\pm \bullet \boldsymbol{\tau}^*)R_\pm = \tau_z$ with $\hat{\mathbf{n}}_\pm \equiv \mathbf{n}_\pm/|\mathbf{n}_\pm|$. The first and second column of R_+ (R_-), respectively, represent the wavefunction of HH and LH on the basis of hole states with spin +3/2 (−3/2) and −1/2 (+1/2). The first (second) component of the quantity $R_\pm^{\dagger}\mathbb{D}_\pm \equiv (\mathfrak{D}_{\mathrm{HH},\pm}, \mathfrak{D}_{\mathrm{LH},\pm})^T$ represents the dipole matrix elements between E and HH (LH) bands. The acceleration process is described by the dynamic phase $A_{\mathrm{HH(LH)}}(t', t)$, which contains the quasi-momentum $\mathbf{k}_{t'}(t'') = e\mathbf{F}_{\mathrm{THz}}(\sin\omega t' - \sin\omega t'')$ satisfying the initial condition $\mathbf{k}_{t'}(t') = \mathbf{0}$ indicated by the subscript t' and $\hbar\partial_{t''}\mathbf{k}_{t'}(t'') = -e\mathbf{E}_{\mathrm{THz}}(t'')$, with e being the elementary charge and $\mathbf{E}_{\mathrm{THz}}(t) = \mathbf{F}_{\mathrm{THz}}\cos\omega t$ the THz electric field.

The three-step process of HSG can thus be described as interference of the following recollision pathways: a Bloch wave associated with an electron–hole pair E–HH (E–LH) is first created by the NIR laser with amplitude proportional to $\mathfrak{D}_{\mathrm{HH(LH)},\pm}\cdot\mathbf{E}_{\mathrm{NIR}}(t')$, acquires a dynamic phase $A_{\mathrm{HH(LH)}}(t',t)$ during the acceleration phase from t' to t, and generates sidebands through the dipole vector $\mathfrak{D}_{\mathrm{HH(LH)},\pm}$. The major contribution to the sideband amplitudes comes from the recollision pathways around the saddle-points (t',t) given by the stationary-phase conditions:

$$-\hbar\frac{\partial A_{\mathrm{HH(LH)}}(t',t)}{\partial t'}+\hbar\Omega$$
$$=\int_{t'}^{t}\mathrm{d}t''\frac{\partial\mathbf{k}_{t'}(t'')}{\partial t'}\cdot(\nabla_{\mathbf{k}}E_{\mathrm{c}}[\mathbf{k}_{t'}(t'')]-\nabla_{\mathbf{k}}E_{\mathrm{HH(LH)}}[\mathbf{k}_{t'}(t'')])=0$$

$$-\hbar\frac{\partial A_{\mathrm{HH(LH)}}(t',t)}{\partial t}=E_{\mathrm{c}}[\mathbf{k}_{t'}(t)]-E_{\mathrm{HH(LH)}}[\mathbf{k}_{t'}(t)]=\hbar\Omega+n\hbar\omega$$

We have used the condition $E_{\mathrm{c}}(\mathbf{0})-E_{\mathrm{HH(LH)}}(\mathbf{0})=E_{\mathrm{g}}=\hbar\Omega$, where E_{g} is the bandgap. Substituting the energy dispersion relations $E_{\mathrm{c}}(\mathbf{k})=E_{\mathrm{g}}+\frac{\hbar^2k^2}{2m_{\mathrm{c}}}$ (m_{c} is the effective mass of the conduction band), $E_{\mathrm{HH}}(\mathbf{k})=-\frac{\hbar^2k^2}{2m_{\mathrm{HH}}}$ and $E_{\mathrm{LH}}(\mathbf{k})=-\frac{\hbar^2k^2}{2m_{\mathrm{LH}}}$ ($m_{\mathrm{HH}}=m_0(\gamma_1-2\gamma_2|\mathbf{n}_\pm|)^{-1}$ and $m_{\mathrm{LH}}=m_0(\gamma_1+2\gamma_2|\mathbf{n}_\pm|)^{-1}$ are the effective masses of the HH and LH bands, respectively) into the stationary-phase conditions, we obtain

$$\int_{t'}^{t}\mathrm{d}t''\mathbf{k}_{t'}(t'')=0$$

$$\frac{\hbar^2\mathbf{k}_{t'}^2(t)}{2\mu_{\mathrm{ch(cl)}}}=n\hbar\omega$$

where $\mu_{\mathrm{ch}}=\left(m_{\mathrm{c}}^{-1}+\frac{\gamma_1-2\gamma_2|\mathbf{n}_\pm|}{m_0}\right)^{-1}\left(\mu_{\mathrm{cl}}=\left(m_{\mathrm{c}}^{-1}+\frac{\gamma_1+2\gamma_2|\mathbf{n}_\pm|}{m_0}\right)^{-1}\right)$ is the reduced mass of the E–HH (E–LH) pair. The first equation has the meaning that the electron–hole pairs return to the position where they are created. The second equation states energy conservation at recollision. For each sideband order n, these two equations can be solved for the saddle-points (t',t), which determine k-space trajectories $\mathbf{k}_{t'}(t'')$, as well as classical real-space trajectories with the velocities of E, HH and LH given by $\hbar\mathbf{k}_{t'}(t'')/m_{\mathrm{c}}$, $-\hbar\mathbf{k}_{t'}(t'')/m_{\mathrm{HH}}$ and $-\hbar\mathbf{k}_{t'}(t'')/m_{\mathrm{LH}}$. Figure 1b shows the shortest trajectory for the 24th-order sideband, and parameters $m_{\mathrm{c}}=0.067m_0$, $m_{\mathrm{HH}}=0.711m_0$ and $m_{\mathrm{LH}}=0.081m_0$ are used in the calculation.

Representation of Bloch wavefunctions

The wavefunctions of the Hamiltonian $H_{\mathrm{v}}^{\pm}(\mathbf{k})$ are eigenfunctions of $\hat{\mathbf{n}}_\pm\bullet\boldsymbol{\tau}$, which is defined on the basis of spin $\mp3/2$ and $\pm1/2$ states. We define $\hat{\mathbf{n}}_\pm=(\sin\Theta\cos\Phi,\sin\Theta\sin\Phi,\cos\Theta)$ as a point on a Bloch sphere with polar angle Θ and azimuthal angle Φ, and write the eigenfunctions of $H_{\mathrm{v}}^{\pm}(\mathbf{k})$ as:

$$|\mathrm{HH}_\pm\rangle=\left(\cos\left(\frac{\Theta}{2}\right)\quad \mathrm{e}^{\mathrm{i}\Phi}\sin\left(\frac{\Theta}{2}\right)\right)$$

$$|\mathrm{LH}_\pm\rangle=\left(-\sin\left(\frac{\Theta}{2}\right)\quad \mathrm{e}^{\mathrm{i}\Phi}\cos\left(\frac{\Theta}{2}\right)\right)$$

The point on the Bloch sphere with coordinates $\hat{\mathbf{n}}_\pm$ ($-\hat{\mathbf{n}}_\pm$) represents the state $|\mathrm{HH}_\pm\rangle$ ($|\mathrm{LH}_\pm\rangle$) for the HH (LH) band. The angles Θ and Φ are determined from the measured γ_3/γ_2 and angle θ through the definition $\mathbf{n}_\pm=\left(\frac{\sqrt{3}}{2}\sin(2\theta),\mp\frac{\sqrt{3}\gamma_3}{2\gamma_2}\cos(2\theta),-\frac{1}{2}\right)$.

Data availability

The datasets generated and/or analysed during the current study are available in the Materials Cloud repository[36]. Source data are provided with this paper.

Code availability

The codes used in the data analysis are available at Zenodo[37].

28. Yablonovitch, E., Hwang, D. M., Gmitter, T. J., Florez, L. T., Harbison, J. P. Van der Waals bonding of GaAs epitaxial liftoff films onto arbitrary substrates. *Appl. Phys. Lett.* **56**, 2419–2421 (1990).
29. Cole, G. D. et al. High-performance near- and mid-infrared crystalline coatings. *Optica* **3**, 647–656 (2016).
30. Yablonovitch, E., Gmitter, T., Harbison, J. P., Bhat, R. Extreme selectivity in the lift-off of epitaxial GaAs films. *Appl. Phys. Lett.* **51**, 2222–2224 (1987).
31. Cole, G. D., Zhang, W., Martin, M. J., Ye, J., Aspelmeyer, M. Tenfold reduction of Brownian noise in high-reflectivity optical coatings. *Nat. Photon.* **7**, 644–650 (2013).
32. Wilmer, B. L., Webber, D., Ashley, J. M., Hall, K. C., Bristow, A. D. Role of strain on the coherent properties of GaAs excitons and biexcitons. *Phys. Rev. B* **94**, 075207 (2016).
33. Kaminski, J. P. et al. Far-infrared cavity dump coupling of the UC Santa Barbara free-electron laser. *Appl. Phys. Lett.* **57**, 2770–2772 (1990).
34. Takahashi, S., Ramian, G., Sherwin, M. S. Cavity dumping of an injection-locked free-electron laser. *Appl. Phys. Lett.* **95**, 234102 (2009).
35. Voon, L. C. L. Y. & Willatzen, M. *The k·p Method: Electronic Properties of Semiconductors* (Springer Science & Business Media, 2009).
36. Costello, J. B. et al. Reconstruction of Bloch wavefunctions of holes in a semiconductor. *Materials Cloud Archive 2021.113* https://doi.org/10.24435/materialscloud:m0-t8 (2021).
37. Banks, H. B., Valovcin, D. C., O'Hara, S. D. & Costello, J. B. SherwinGroup/HSG-turbo: 2021 release. *Zenodo* https://doi.org/10.5281/zenodo.5116718 (2021).

Acknowledgements We acknowledge R. B. Liu and M. Kira for reading an earlier version of the manuscript; G. Cole and P. Heu for assistance with GaAs membrane fabrication; A. Peñaloza for assistance with the design and fabrication of cryostat modifications; C. Cannon for implementing software for Monte Carlo error estimation; D. Enyeart and N. Agladze for assistance with maintaining and operating the UCSB millimetre-wave free-electron laser; and J. Meyer and I. Vurgaftman for a discussion. The portion of this research conducted at UCSB was funded by NSF-DMR 1710639 and NSF-DMR 2004995. Upgrades to the UCSB terahertz facility that was used for this research were funded by NSF-DMR 1626681 and NSF-DMR 1126894. The portion of this research conducted at Princeton was funded in part by the Gordon and Betty Moore Foundation's EPiQS Initiative, Grant GBMF9615 to L.N.P., and by the National Science Foundation MRSEC grant DMR 1420541.

Author contributions Performing experiments, data collection and analysis: S.D.O. and J.B.C. Software: J.B.C., D.C.V. and S.D.O. Theory: Q.W. Conceptualization: M.S.S. and Q.W. Resources (GaAs epilayer growth): K.W.W. and L.N.P. Development of broad-band polarimetry: D.C.V. Writing: M.S.S., Q.W., S.D.O. and J.B.C. Supervision, funding acquisition and project administration: M.S.S.

Competing interests The authors declare no competing interests.

Additional information
Extended data is available for this paper at https://doi.org/10.1038/s41586-021-03940-2.
Supplementary information The online version contains supplementary material available at https://doi.org/10.1038/s41586-021-03940-2.
Correspondence and requests for materials should be addressed to M. S. Sherwin.
Peer review information *Nature* thanks the anonymous reviewers for their contribution to the peer review of this work. Peer reviewer reports are available.
Reprints and permissions information is available at http://www.nature.com/reprints.

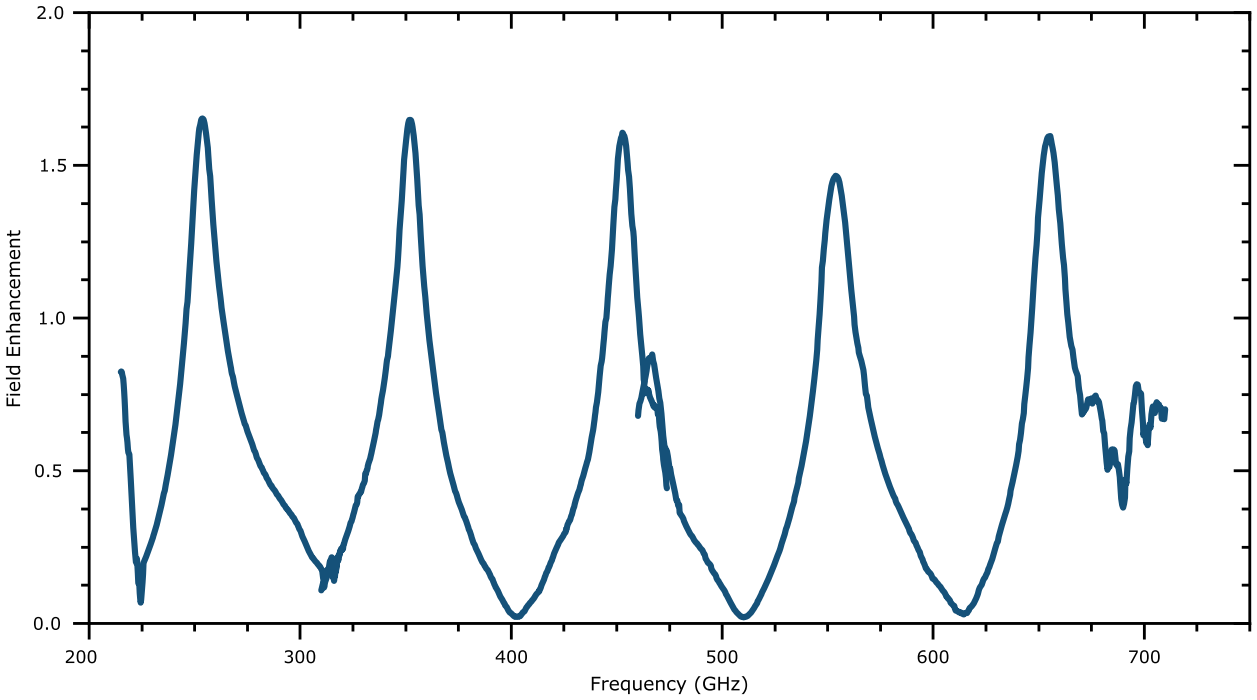

Extended Data Fig. 1 | Field enhancement at the GaAs epilayer from the ITO-coated sapphire substrate. The field enhancement is calculated as $|1 + r(f_{\mathrm{THz}})|$ with the complex reflection coefficient $r(f_{\mathrm{THz}})$ measured by a Vector Network Analyzer.

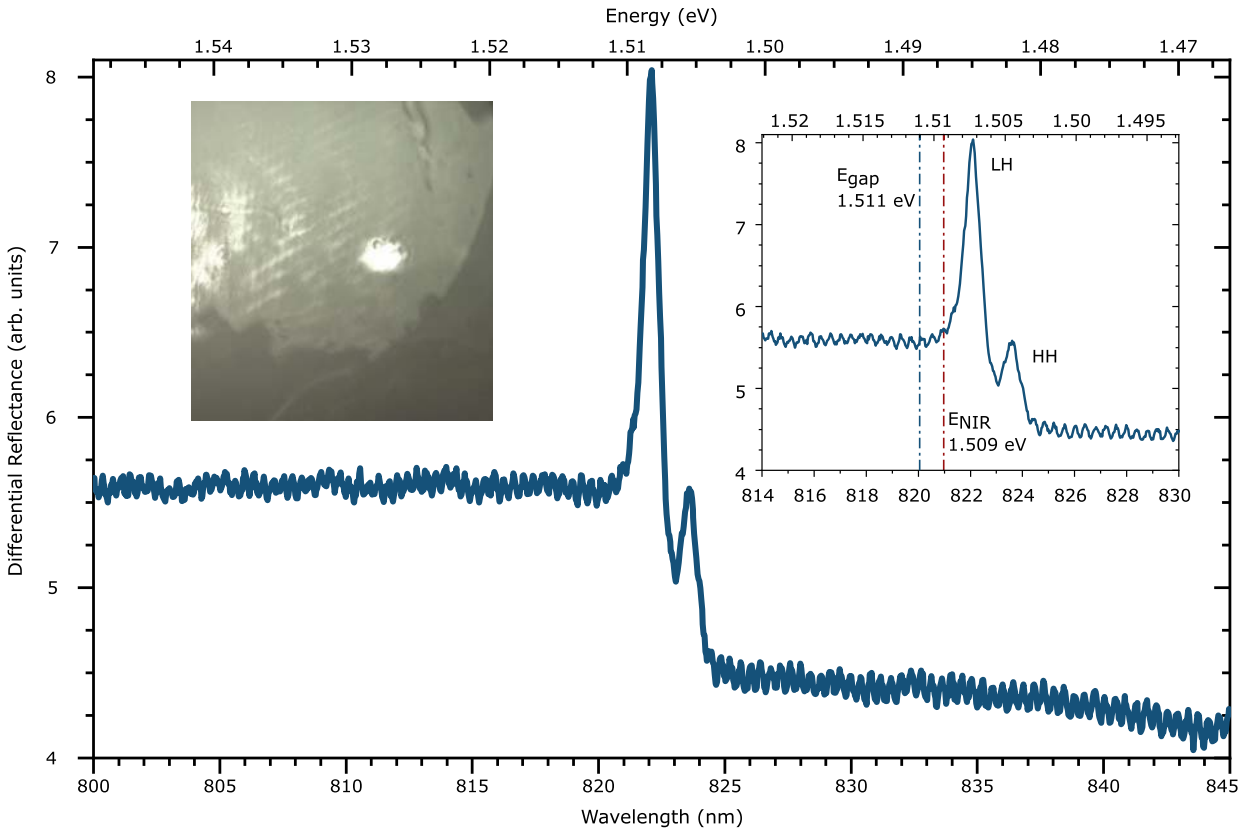

Extended Data Fig. 2 | An absorbance spectrum of the GaAs epilayer mounted on the ITO-coated sapphire substrate. The measurement was taken at the spot illuminated by a white light source (left inset). The right inset shows a zoom-in of the spectrum, with the bandgap and the photon energy of the NIR laser denoted by dash-dot blue and red lines, respectively. The two peaks are strain-split exciton resonances associated with band-edge states with different angular momenta. The temperature was 60 K.

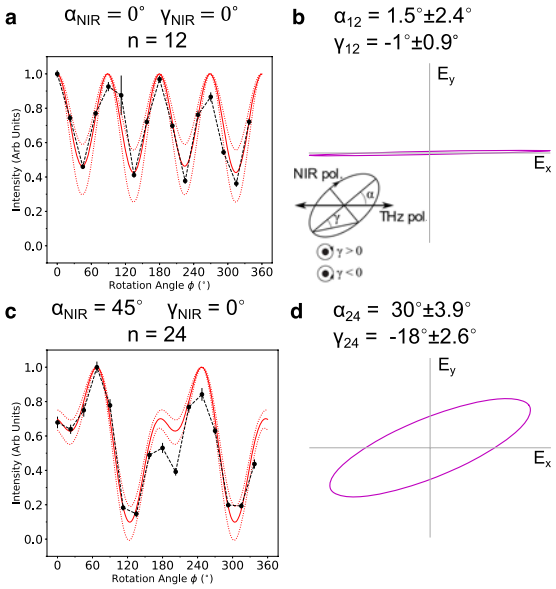

Extended Data Fig. 3 | Stokes polarimetry with linearly polarized NIR laser ($\gamma_{NIR} = 0°$). **a**, Polaragrams for sideband index $n = 12$ and orientation angle of the NIR laser $\alpha_{NIR} = 0°$. **b**, The polarization state of the sideband extracted from the polaragrams in **a**. **c**, Polaragrams for sideband index $n = 24$ and orientation angle of the NIR laser $\alpha_{NIR} = 45°$. **d**, The polarization state of the sideband extracted from the polaragrams in **c**. In **a** and **c**, the black dots show the measured polaragrams, with error bars showing the standard deviation over 4 measurements, and the red solid lines are the reconstructed polaragram through Fourier transform, with the red dotted lines showing the bounds. In **b** and **d**, the polarization states of the sidebands are represented as trajectories of the tips of the electric field vectors (E_x, E_y) over time. The orientation angle α and ellipticity angle γ are defined in the inset in **b**.

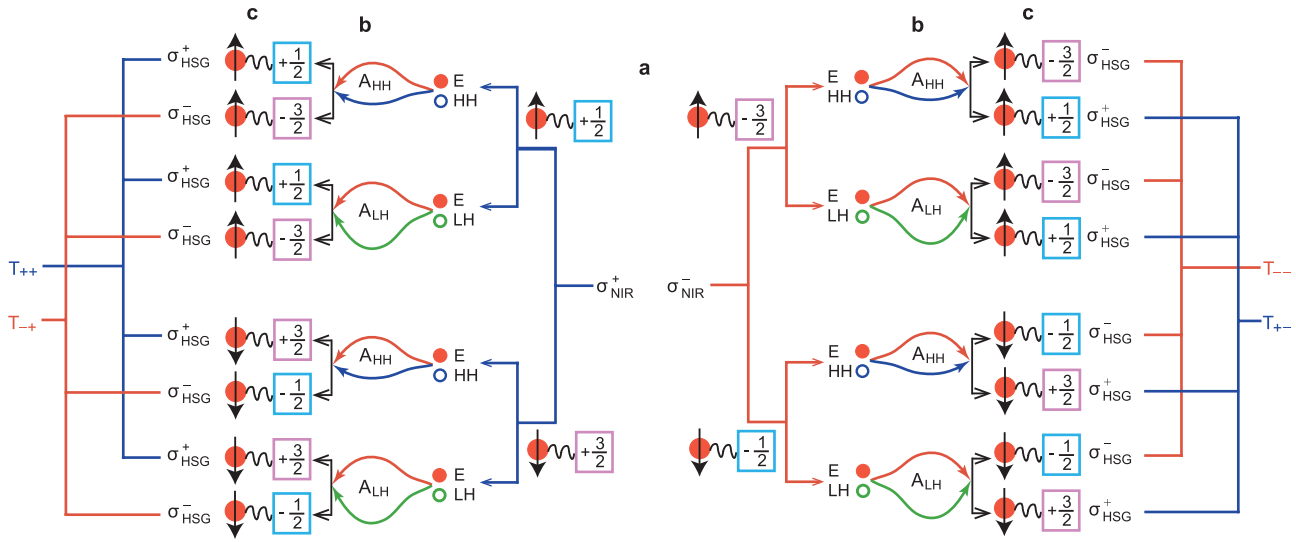

Extended Data Fig. 4 | Quantum interference in three-step model of HSG leading to sideband polarization. A photon from the NIR laser is decomposed into components $\sigma^{\pm}_{NIR}$, with helicity ±1. **a**, A σ^{-}_{NIR} photon excites either a spin-up electron and hole of spin −3/2 or a spin-down electron and hole of spin −1/2. A σ^{+}_{NIR} photon excites either a spin-up electron and hole of spin +1/2 or a spin-down electron and hole of spin +3/2. **b**, Driven by the THz field, an electron-hole pair accumulates dynamic phase A_{HH} or A_{LH}, depending on the band of the hole state (HH or LH). The electron spin is unchanged, while the hole states originating from the spin −3/2 state are superpositions of spin −3/2 and +1/2 states and the states originating from the spin −1/2 state are superpositions of spin −1/2 and +3/2 states. **c**, Upon recollision, either σ^{+}_{HSG} or σ^{-}_{HSG} photons are produced following angular momentum conservation—for example, a spin +3/2 hole recombining with a spin-down (−1/2) electron produces a σ^{+}_{HSG} photon with helicity +3/2 −1/2 = +1. The interference of the evolution pathways from $\sigma^{\pm}_{NIR}$ to σ^{+}_{HSG} (σ^{-}_{HSG}) produces the dynamical Jones matrix element $T_{+\pm}$ ($T_{-\pm}$).

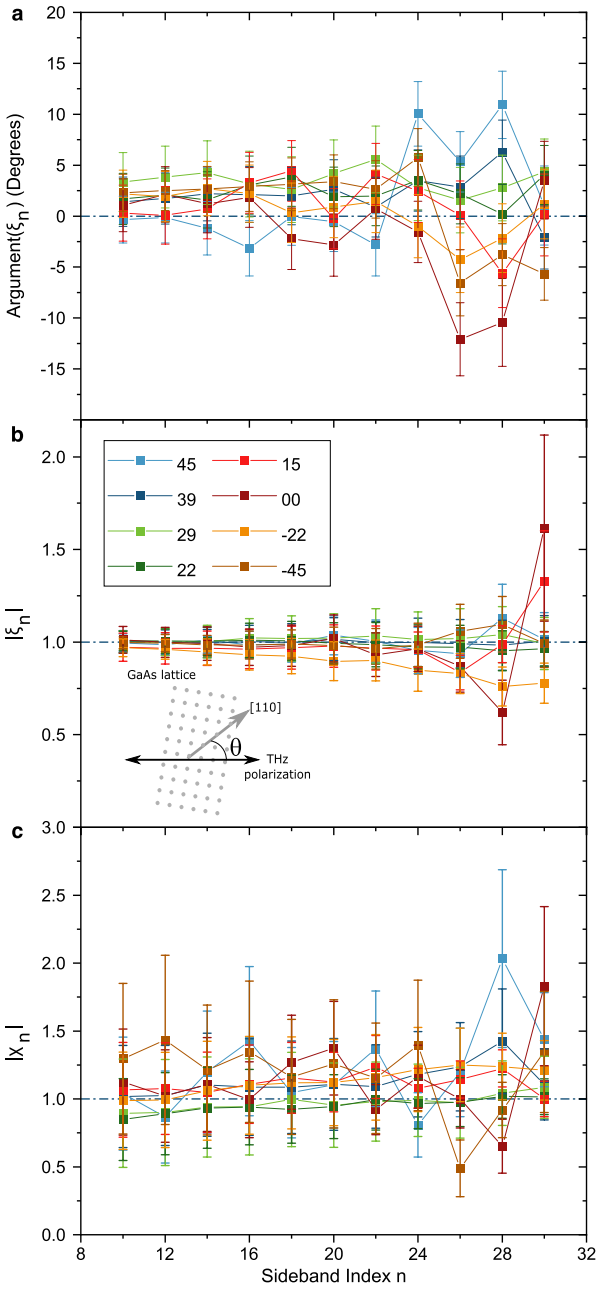

Extended Data Fig. 5 | Additional data for ratios of Jones matrix elements, $\xi_n(\theta)$ and $\chi_n(\theta)$. **a**, The argument of $\xi_n(\theta)$. The dash-dot line marks the expected value of 0. **b**, The magnitude of $\xi_n(\theta)$. The dash-dot line marks the expected value of 1. **c**, The magnitude of $\chi_n(\theta)$. The dash-dot line marks the expected value of 1. All quantities are presented as functions of sideband index n for eight values of angle θ. Inset, The definition of θ by using the GaAs crystal lattice and the THz electric field.

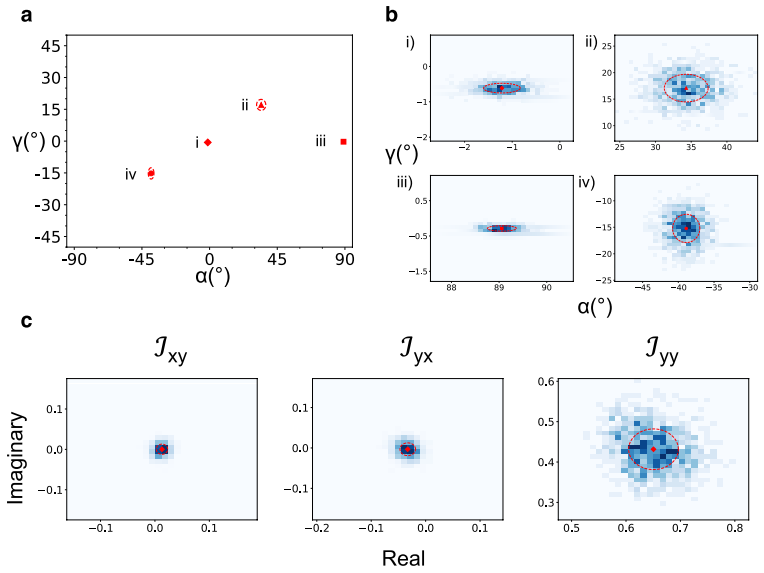

Extended Data Fig. 6 | Monte Carlo simulation in calculating the dynamical Jones matrices. a, The polarization state of the $n = 12$ sideband ($\theta = 23°$) for all 4 initial NIR polarizations (i-$\alpha_{NIR} = 0°$, ii-$\alpha_{NIR} = 45°$, iii- $\alpha_{NIR} = 90°$, iv- $\alpha_{NIR} = -45°$). The horizontal and vertical axes represent α and γ, respectively. Dashed ovals correspond to confidence intervals in the measurement of α and γ. **b**, Histograms of α and γ for the 4 measured sidebands' polarizations. Normal distributions of α and γ were sampled, with the central value and standard deviation of the distributions set by the measured values. In this figure, 1,000 iterations are shown, but the results of this paper are calculated from 10,000 iterations. **c**, The complex $\mathcal{J}$-matrix elements resulting from the α and γ in **b**. The horizontal and vertical axes represent the real and imaginary part, respectively. Each red dashed line shows one standard deviation of the distribution of each $\mathcal{J}$-matrix element resulting from the Monte Carlo simulation. All three plots have the same scale. The value of $\mathcal{J}_{xx,n}$ is set as 1 in these calculations.

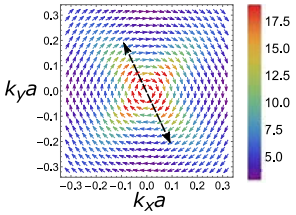

Extended Data Fig. 7 | Berry connection matrix element $\mathcal{A}_{HH_+,HH_+}$ in the $k_z = 0$ plane of the Brillouin zone. The double-headed black dotted arrow represents a path of a hole accelerated by a linearly polarized THz field, which is perpendicular to the Berry connection (color arrows) at all points. The Berry connection is plotted in units of a, which is the lattice constant of GaAs.

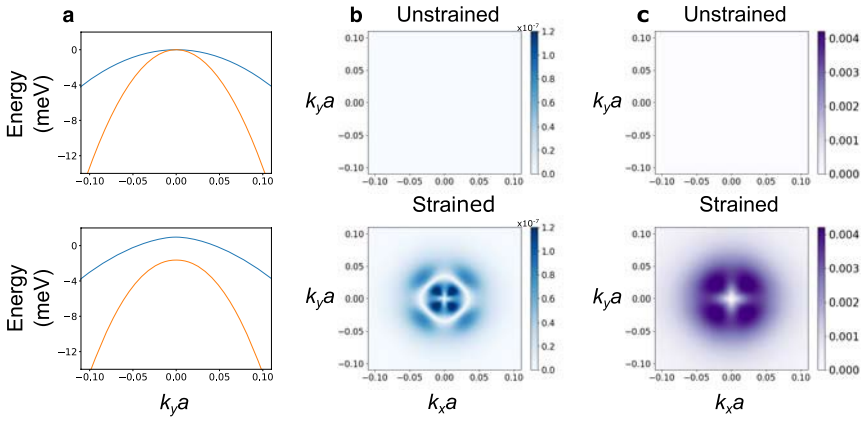

Extended Data Fig. 8 | Effect of a biaxial strain on the valence band structure and non-Abelian Berry connection along the direction of quasi-momentum $\boldsymbol{k}$ in the $\boldsymbol{k_z}$ = 0 plane of the Brillouin zone. The strain is chosen as tensile along [001] direction to be consistent with the splitting of the exciton peaks in the absorbance spectrum (Extended Data Fig. 2). **a**, Valence band structures along $k_x = k_z = 0$ for unstrained (top) and strained (bottom) GaAs. The blue and orange curves represent the heavy-hole and light-hole bands, respectively. **b**, The magnitude of the diagonal Berry connection matrix element $\mathcal{A}_{HH_+,HH_+}$ along the direction of quasi-momentum for unstrained (top) and strained (bottom) GaAs. **c**, The magnitude of the off-diagonal Berry connection matrix element $\mathcal{A}_{HH_+,LH_+}$ along the direction of quasi-momentum for unstrained (top) and strained (bottom) GaAs. For the unstrained case, the Berry connection along the quasi-momentum is identically zero in the plots except for the singularity at $\boldsymbol{k}$=**0**. The Berry connection is plotted in units of a, which is the lattice constant of GaAs.